Carbon 205 (2023) 394–401

Contents lists available at ScienceDirect

Carbon

journal homepage: www.elsevier.com/locate/carbon

Research paper

Universality of moiré physics in collapsed chiral carbon nanotubes

Olga Arroyo-Gascón [a,b], Ricardo Fernández-Perea [c], Eric Suárez Morell [d], Carlos Cabrillo [c], Leonor Chico [b,*]

[a] Instituto de Ciencia de Materiales de Madrid, Consejo Superior de Investigaciones Científicas, C/ Sor Juana Inés de la Cruz 3, 28049 Madrid, Spain
[b] GISC, Departamento de Física de Materiales, Universidad Complutense, E-28040 Madrid, Spain
[c] Instituto de Estructura de la Materia (IEM), CSIC, Serrano 123, E-28006 Madrid, Spain
[d] Departamento de Física, Universidad Técnica Federico Santa María, Casilla 110-V, Valparaíso, Chile

ARTICLE INFO

Keywords:
Carbon nanotubes
Moiré
Magic angles
Twisted bilayer graphene

ABSTRACT

We report the existence of moiré patterns and magic angle physics in all families of chiral collapsed carbon nanotubes. A detailed study of the electronic structure of all types of chiral nanotubes, previously collapsed via molecular dynamics, has been performed. We find that each family possesses a unique geometry and moiré disposition, as well as a characteristic number of flat bands. Remarkably, all kinds of nanotubes behave the same with respect to magic angle tuning, showing a monotonic behavior that gives rise to magic angles in full agreement with those of twisted bilayer graphene. Therefore, magic angle behavior is universally found in chiral collapsed nanotubes with a small chiral angle, giving rise to moiré patterns. Our approach comprises first-principles and semi-empirical calculations of the band structure, density of states and spatial distribution of the localized states signaled by flat bands.

1. Introduction

In recent years, layered materials showing moiré patterns have stood as a platform for the exploration of new physics [1–9]. Graphene-based materials, such as twisted bilayer graphene (TBG) and transition metal dichalcogenides, constitute two families of great interest. In particular, layered graphene structures have been shown to host electronic correlations, superconductivity and nontrivial topological phases when arranged at a small rotation angle, the so-called magic angle, which is close to 1° for TBG [4,5,10–14].

The quest for novel materials which could enlighten these new phenomena has even extended to one-dimensional systems, where many-body effects have been widely described. Flat bands can be found in some one-dimensional materials [15–18]; for instance, carbon nanotubes (CNT) can show moiré patterns in their double-walled and multi-walled form [19–21], and single-walled tubes also display moirés when collapsed [17]. For the latter, flat bands with an even smaller energy span than TBG and sharp densities of states ensue along with these one-dimensional patterns. As in TBG, these features depend on the rotational angle, which is related to a corresponding chiral angle in collapsed CNTs.

The electronic structure of carbon nanotubes is varied, comprising metallic and semiconducting tubes. In metallic CNTs, which host Dirac fermions as in graphene, the Dirac point can be located at the center of the Brillouin zone (the Γ point) or at 2/3 of the Γ-X line [22]. We denote them as Γ-metals and 2/3-metals, respectively [17]. Chiral metallic CNTs can belong to these two groups, although a small gap develops due to curvature effects. In a previous article, we found flat bands and highly localized states in the AA regions (zones of AA stacking) of the moiré patterns formed in collapsed 2/3-metal nanotubes with small chiral angles [17]. In that work we chose to explore 2/3-metallic CNTs because of their similarity to graphene: they present two bands with linear dispersion crossing at 2/3 of the positive part of their Brillouin zone, being the one-dimensional (1D) analogues of the Dirac cones in graphene. However, the behavior of collapsed chiral Γ-metals and semiconducting tubes is yet unknown; further analysis is needed to elucidate whether magic angle physics also pertains to the rest of families of chiral tubes.

In order to obtain CNTs that are stable upon collapse with sizeable moirés at small chiral angles, tubes with diameters above 40 Å, often involving a high number of atoms per unit cell, are needed [23–32]. Note that for free-standing collapsed nanotubes the threshold is higher, 51 Å [30,31], although deposition on a substrate can lower this limit substantially [32]. The search for Γ-metal and semiconducting tubes which fulfill these conditions leads to nanotubes showing several AA regions per unit cell, which is intrinsically related to the symmetry operations and the number of localized states in the structure.

* Corresponding author.
E-mail addresses: o.arroyo.gascon@csic.es (O. Arroyo-Gascón), leochico@ucm.es (L. Chico).

https://doi.org/10.1016/j.carbon.2023.01.052
Received 9 November 2022; Received in revised form 24 January 2023; Accepted 26 January 2023
Available online 30 January 2023

In this work, we show that moiré physics occurs for all collapsed chiral carbon nanotubes close to the magic angle, regardless of their metallic or semiconducting behavior. We assess several criteria usually employed to describe magic angle physics: the appearance of flat bands and the reduction of the Fermi velocity, sharp peaks in the density of states, and real-space electronic localization via local density of states [1,4,17,33]. We study the interplay of these criteria and discuss the most suitable one for our system. Analyzing these benchmarks, we perform an exhaustive description of the electronic structure of a range of collapsed chiral nanotubes belonging to each family: semiconducting, 2/3-metals and Γ-metals.

We find a magic angle very close to that of TBG for the three families of CNTs, namely, 1.12° for 2/3-metals, and 1.11° for semiconducting and Γ-metals. Moreover, a homogeneous behavior extends to all tubes when their moiré angle is small enough, regardless of their specific family or symmetries. Our findings imply that the experimental observation of one-dimensional moiré physics in CNTs might be easier than previously expected.

2. Geometry and symmetry

Let us briefly recall the standard notation in nanotube physics. CNTs are identified by its circumference vector $\boldsymbol{C_h}$ on an unrolled graphene sheet. The coordinates of $\boldsymbol{C_h}$ in the graphene basis, (n, m), are customarily used to label CNTs. Considering a one-orbital model and leaving out curvature effects, if $n - m$ is a multiple of 3, the tube is metallic [34–36]. Another important magnitude is the chiral angle of the CNT, θ_{NT}, which is spanned between the $(n, 0)$ direction and $\boldsymbol{C_h}$. Upon collapsing a chiral carbon nanotube, a moiré pattern can emerge, which is directly related to the CNT chiral angle θ_{NT}. Thus, a moiré angle θ_M can be defined as the relative rotation angle between the two flattened parts of the CNT, just as in TBG. An analysis of the geometry of the unrolled unit cell yields $\theta_M = 2\theta_{NT}$ [17], so that in the following tubes will be labeled by the angle θ_M.

Addressing a wider range of nanotube types implies that new tube symmetries may be involved. Since the geometry of each tube is related to its symmetry operations, the existence and arrangement of moiré patterns once the structure is collapsed can be predicted. Line groups describe the symmetry operations of one-dimensional systems, such as CNTs. Specifically, chiral cylindrical nanotubes belong to the fifth line group and comprise screw-axis and isogonal point group D_p symmetries, where p is the greatest common divisor of the nanotube indices n and m [37]. Dihedral groups include rotations and often reflections; in particular, a rotational C_{2q} symmetry operation, where q is an integer, is convenient, so to obtain two equivalent graphene regions on the unrolled unit cell, that will constitute the two coupled "layers" of the collapsed nanotube yielding a full AA moiré area. In fact, this is the simplest symmetry that yields full AA moiré patterns once the tube is collapsed. This rotational symmetry can be achieved by choosing nanotubes with indices $(2m, 2)$. We have followed this method for 2/3-metallic and semiconducting nanotubes; despite having the same greatest common divisor p, 2/3-metals and semiconducting tubes might not have the same symmetry operations and exhibit different moiré patterns. In fact, as it is shown in Fig. 1(a), a C_2 symmetry not only can render one centered AA moiré region per unit cell as in 2/3-metals, but three.

As for Γ-metallic CNTs, they usually have more atoms per unit cell than semiconducting chiral CNTs with similar chiral angles. Suitable nanotubes should be at least 40 Å-wide so that they are stable once collapsed. The smallest tubes that fulfill the aforementioned diameter condition and have a moiré angle close to the magic angle in TBG have indices $(3m, 3)$, thus showing C_3 symmetry. This results on a zigzag arrangement of the AA moiré regions with respect to the tube axis (see Fig. 1(b)), in contrast to the linear disposition achieved for 2/3-metallic and semiconducting tubes. The minimum number of AA regions per unit cell for these tubes is now six (taking into account half AA moiré spots). Therefore, we show that not only C_{2q}-symmetric tubes are suitable for moiré engineering, and that sizeable AA regions can appear in all families of CNTs.

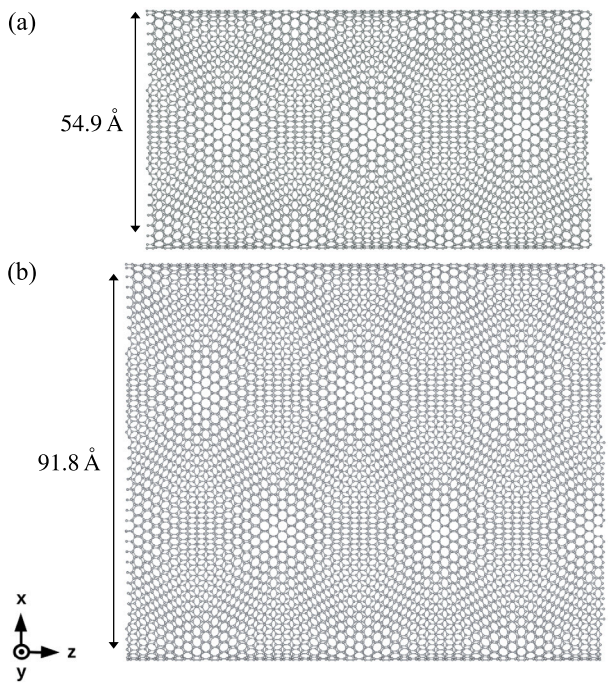

Fig. 1. Top view of the unit cells of the (a) collapsed semiconducting (48,2) and (b) Γ-metal (78,3) nanotubes. The number and placement of the AA regions differ and depend on the symmetry operations of the original cylindrical tube.

The appearance of AA-stacked moiré patterns in the center of collapsed chiral tubes, such as in TBG, motivates the search for fragile topological phases in CNTs, that have been predicted and found in TBG [11,12] and other systems displaying flat bands [38]. For instance, edge states in cylindrical CNTs can be classified attending to a topological invariant [39]. However, a group theory analysis of the band representations following [40] does not render fragile topology [41]. Regarding collapsed CNTs, the molecular dynamics process can break the rotational symmetries of the tubes, so that symmetry-protected fragile topological states, such as C_2T in TBG [11], are not feasible in our case. Nevertheless, model Hamiltonians used to describe nontrivial topology in TBG could be applied to the central part of our tubes, where the AA regions appear, since C_2 symmetry is locally present there.

3. Methods

Collapsed nanotubes are simulated by means of molecular dynamics calculations, resorting to the Large-scale Atomic/Molecular Massively Parallel Simulation (LAMMPS) package [42]. This allows us to have a reliable description of the structure. In fact, at low angles we reproduce the corrugations that are known to appear in TBG [43] in the flattened, bilayer-like portion of the nanotubes. An Adaptive Intermolecular Reactive Empirical Bond Order (AIREBO) [44] potential models the interactions between carbon atoms. Periodic conditions are applied with supercells wide enough to avoid interaction between nanotube replicas. A detailed description of the methods used in this work can be found in the Supporting Information of [17]. Fig. 1 shows two examples of converged final geometries.

The band structure of the tubes is then obtained by means of a tight-binding model derived from that presented by Nam and Koshino [45]:

$$H = -\sum_{i,j} t(\mathbf{R}_i - \mathbf{R}_j)|\mathbf{R}_i\rangle\langle\mathbf{R}_j| + \text{H.}c., \tag{1}$$

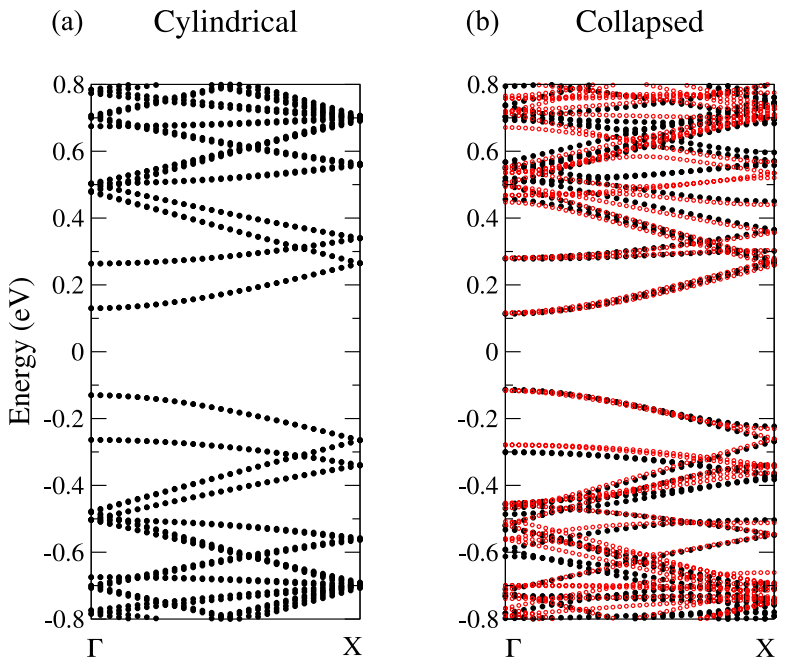

Fig. 2. Band structures of the (36,2) CNT with $\theta_M = 5.36°$: (a) for the cylindrical geometry, obtained with the tight-binding model; (b) for the collapsed structure, obtained with both tight-binding (black) and DFT (red) calculations. (For interpretation of the references to color in this figure legend, the reader is referred to the web version of this article.)

where $\mathbf{R}_i$ is the position of the atom i, $|\mathbf{R}_i\rangle$ is the wavefunction at i, and $t(\mathbf{R})$ is the hopping between atoms i and j:

$$-t(\mathbf{R}) = V_{pp\pi}(R)\left[1-\left(\frac{\mathbf{R}\cdot\mathbf{e}_y}{R}\right)^2\right] + V_{pp\sigma}(R)\left(\frac{\mathbf{R}\cdot\mathbf{e}_y}{R}\right)^2 \quad (2)$$

The explicit expression of the hopping parameters $V_{pp\pi}(R)$ and $V_{pp\sigma}(R)$ is detailed in the Supporting Information of [17]. After the molecular dynamics calculation, the tubes end up with a flattened central region where moirés appear (see Fig. 1), as well as two narrow lobular regions at the extremes of the flattened part. Both $V_{pp\pi}(R)$ and $V_{pp\sigma}(R)$ contributions are taken into account for the flat part. Only the $V_{pp\pi}(R)$ part of the Hamiltonian is applied to the regions of the lobes, since we do not need to assess the effect of corrugations therein.

The tight-binding Hamiltonian allows us to model nanotubes which would be computationally out of reach within a first-principles approach. In addition, it is validated against DFT calculations of the electronic bands of a relatively small semiconducting tube, namely the (36,2), employing the SIESTA code within the generalized gradient approximation (GGA) using the Perdew–Burke–Ernzerhof (PBE) parameterization [46–48] and a 1 × 1 × 4 Monkhorst–Pack grid sampling of the Brillouin zone. Even though the GGA-PBE formalism in general underestimates the band gap for semiconductors, a hybrid functional approach is not feasible since we are dealing with thousands of atoms per unit cell. Moreover, we have found that most collapsed CNTs near the magic angle are metallic or have a negligible band gap. We are therefore able to compare the first-principles and tight-binding electronic structures of the collapsed tube, where the atomic coordinates are taken from the relaxed nanotube atomic configuration previously obtained by molecular dynamics simulations. Fig. 2 illustrates the agreement between tight-binding (black) and DFT (red) calculations; it is especially important to reflect properly the behavior of the central bands nearest to the Fermi energy, since they will be the most affected upon collapse. Note that the bands of the (36,2) tube, which has 2744 atoms per unit cell, only show a slight flattening since the moiré angle is $\theta_M = 5.36°$, which has to be compared with the magic angle in TBG, $\sim 1.1°$.

4. Benchmarks of magic angle physics in semiconducting and Γ-metal CNTs

4.1. Semiconducting nanotubes

In order to extend the flat band picture from 2/3-metal CNTs to all kinds of tubes, the first family we analyze are semiconducting CNTs. As stated in Section 2, we choose these tubes to present a C_2 symmetry, which produces three AA regions per unit cell, located along the nanotube axis (see Fig. 1(a)). Recall that 2/3-metallic CNTs have been shown to host a set of eight flat bands near the neutrality point along with an inner subset of 4 notably flat bands, and a single AA region per unit cell [17]. Since the number of AA regions per unit cell has now increased, a higher number of bands are expected to be affected by the collapse. Besides, semiconducting tubes fulfilling our requirement also show a higher number of atoms per unit cell compared to 2/3-metal CNTs with a similar moiré angle.

Fig. 3(a) clearly depicts a progressive flattening and isolation of the central bands of several tubes as the moiré angle decreases, ranging from 1.49° to 0.98°. This central set now encompasses 24 bands, instead of the 8 bands found in 2/3-metals. Remarkably, and as in 2/3-metals, a subset of several extremely flat bands is found in the semiconducting tubes. For 2/3-metals, the innermost 4-band set is most flattened; for semiconducting tubes, the number of flat bands in this set increases to 12 and are distinguishable starting from the (162,2) tube in Fig. 3(a). Hence, the number of flattened bands in semiconductors is triple than in 2/3-metals; this is ultimately related to the number of AA regions per unit cell, which is also triple.

Semiconducting tubes can be divided in two groups depending on whether the relation between their indices $n - m = 3l \pm 1$, where l is an integer; for instance, the (132,2) and (162,2) tubes belong to the +1 group whereas the (172,2) and (202,2) tubes belong to the −1 subfamily. They have been shown to display different optical and electronic properties [49–51], so it is reasonable to ask whether such differences may arise with respect to moiré physics. However, observing Fig. 3(a) we find that the ±1 classification does not have a significant effect on the flattening of the central bands of the tubes.

We previously found [17] that in 2/3-metals, as in TBG, flat bands give rise to sharp signals of electronic localization in the density of

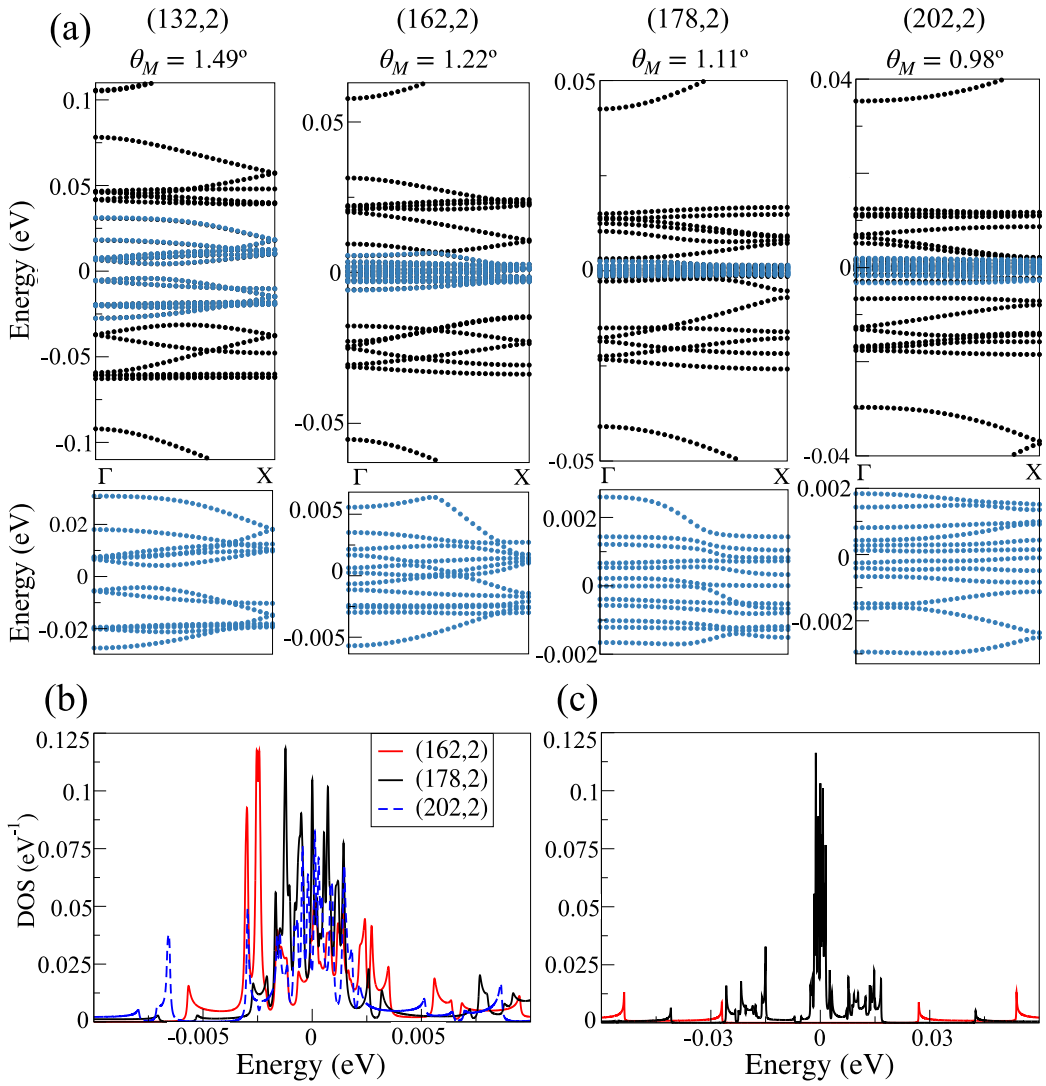

Fig. 3. (a) Band structures of four semiconducting collapsed tubes; the innermost 12 bands are highlighted in blue and presented in zoom-ins in the bottom panel. Notice the different energy scales. (b) Density of states of the largest three semiconducting tubes in panel (a). (c) Comparison between the collapsed (black) and cylindrical (red) DOS for the (178,2) tube, which displays the maximum peak height among the depicted tubes. (For interpretation of the references to color in this figure legend, the reader is referred to the web version of this article.)

states (DOS). This is a consequence of the proportionality of the DOS with the inverse of the norm of the electronic velocity integrated over the energy surface. In our 1D case, such a relation is inversely proportional to the electronic speed, so that the DOS per atom reads,

$$\rho(\varepsilon) = \frac{1}{\rho_A D_{cnt}} \sum_n \frac{1}{\hbar\,|v_n(k)|_{k=k_n(\varepsilon)}}\,, \tag{3}$$

where n labels the electronic bands, $v_n(k)$ is the corresponding electron velocity, ρ_A is the carbon areal density of graphene, and D_{cnt} the diameter of the CNT. Expression (3), since $\hbar\,|v_n(k)|$ is the derivative of the band dispersion relation, neatly illustrates that flattening of the bands gives rise to high narrow peaks in the DOS. The presence of higher and narrower peaks is a signature of higher localization, and thus, of a larger probability of strongly correlated electronic behavior. Comparing the DOS peak heights thus serves as a criterion for the potential for strong electronic correlations among diverse nanotubes. Additionally, Eq. (3) also implies that for a given resolution the DOS is proportional to the inverse of the electronic velocity averaged over the resolution function. But notice that if, alternatively, we choose as localization criterion the vanishing of electronic velocities in absolute terms, the heights we must compare are those of the DOS multiplied by the corresponding nanotube diameter. All the DOS presented in this work have been computed with a 50 μeV Lorentzian resolution (energy broadening).

Fig. 3(b) shows the DOS for the largest semiconducting tubes in Fig. 3, computed from the dispersion relations. Due to the flattening, these tubes become metallic and sharp peaks appear near the neutrality point, whereas a small gap is observed for smaller tubes. As the moiré angle decreases, the peaks pack together around the Fermi level. Moreover, the innermost 12-band set is also separated from the rest of the spectrum. The maximum DOS peak height is reached for the (178,2) tube, with an angle $\theta_M = 1.11°$. Multiplying by the corresponding diameters does not change the qualitative picture but enhances the preponderance of the (178,2) tube.

The effect of collapse on the DOS is illustrated in Fig. 3(c), which spans the 16 innermost bands of the (178,2) tube, both cylindrical and collapsed. The former spaced bands in the cylindrical structure gather around the Fermi level upon collapse and give rise to pronounced peaks that evidence the high localization of these states. As the LDOS for the smaller (94,2) CNT displayed in Fig. 4 confirms, the states are also localized in the AA regions. These three AA-stacked regions show equal enhancement of the DOS, consistently with the triple number of

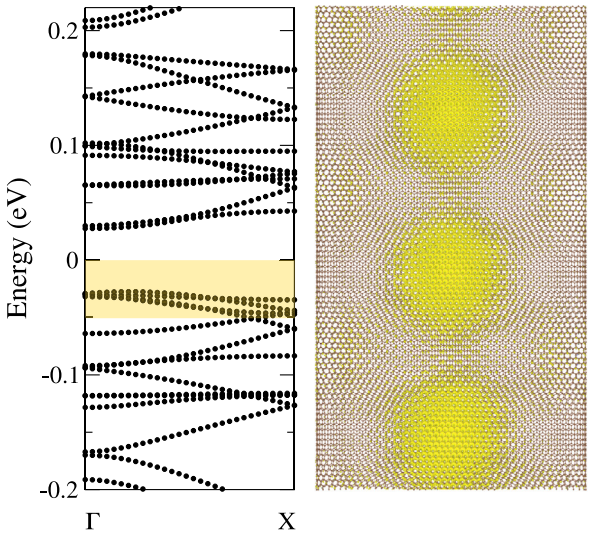

Fig. 4. Band structure and top view of the (94,2) collapsed semiconducting nanotube. The LDOS of the marked bands is highlighted in yellow. (For interpretation of the references to color in this figure legend, the reader is referred to the web version of this article.)

flat bands present in these tubes with respect to those found in 2/3-metals. Notice also that electron–hole symmetry breaks when the tube is flattened due to the interlayer hopping in our model.

Even though the DOS criterion highlights the (178,2) tube, analyzing the energy span of the tubes depicted in Fig. 3 we find that the energy spans for the (178,2) tube are 0.2 meV and 0.52 meV for the lower conduction and highest valence band respectively (conduction band and valence band from now on), larger than those of the (202,2) tube (0.04 meV and 0.15 meV respectively). Therefore, for semiconducting nanotubes, the DOS and the band span criteria point to different nanotubes.

4.2. Γ-Metal nanotubes

Γ-metal tubes are similar to 2/3-metals, in that they both display a Dirac-like dispersion that is renormalized upon collapse. However, the smaller suitable Γ-metals show six AA regions per unit cell instead of one (see Fig. 1(b)). Although the number of AA regions per unit cell is six times that of the 2/3-metals, that does not necessarily mean sextuple localized states: comparing Fig. 1(a) and (b), it follows that the symmetry of Γ-tubes is different to that of 2/3-metallic and semiconducting tubes in a way that precludes the tube structure to be approximated by consecutive copies of single-AA-region cells, as it is the case with semiconducting CNTs.

As depicted in Fig. 5(a), the Dirac crossing is slightly displaced away from the Γ point for the collapsed tubes. This Figure is equivalent to Fig. 3(a) but for Γ-metals, with moiré angles between 1.49° and 0.95°. The bands constituting the Dirac cone are only distinguishable in the leftmost panel. Overall, a set of 36 bands are progressively isolated and flattened, with an inner set of 24 very flat bands. This subset has certainly sextuple bands that the equivalent set in 2/3-metals, in spite of the above-mentioned different symmetry. And indeed, the states are again equally localized at the six AA regions, as Fig. 6 illustrates. Therefore, one can establish for all kinds of nanotubes a direct proportionality between the number of AA regions and the number of flat bands around the neutrality point that appear at small chiral angles.

Fig. 5(b) shows the corresponding DOS of the three largest tubes. The most prominent peak appears in the (267,3) case with a moiré angle of $\theta_M = 1.11°$. The cluster of narrowest peaks show this time a bimodal structure around the Fermi level, i.e., the bands nearest to Fermi are not particularly flat, something that can be gauged also in the band plots (zooms in Fig. 5(a)).

As in the semiconductors, the smallest energy span among Γ-metals does not correspond to the case with the most prominent DOS peak. In particular, the (312,3) tube (moiré angle $\theta_M = 0.95°$) has 0.16 meV and 0.06 meV energy spans for conduction and the valence bands respectively, to be compared with 0.27 meV and 0.16 meV in the case of the (267,3) tube.

4.3. Global discussion and analysis for all CNT types

Fig. 7 gives a general picture of the band flattening in collapsed chiral carbon nanotubes in terms of the energy spans of their bands around the Fermi level. The widths of all band sets decrease gradually (with a similar trend) as the moiré angle diminishes independently of the family each tube belongs to. This picture neatly illustrates that a small moiré angle is the only requirement needed to obtain flat bands in all types of collapsed chiral nanotubes. Band spans of the whole central sets are in agreement with those of TBG, taking into account folding effects [45].

With respect to the degree of the localization, Fig. 8 displays the best DOS results for the three main types of nanotubes (as mentioned earlier, there is no observed distinction between the two kinds of semiconductors). At the magic angle, the most prominent peak of the 2/3-metal is substantially higher than those of the other cases. The 2/3-metallic tube also has the most centered and narrower distribution of peaks around the Fermi level. Such narrowing is to be expected, since the group of flattest bands is only four here. We already know that the number of bands that undergo this flattening with diminishing chiral angle correlates with the number of AA-regions in the corresponding moiré pattern of a primitive cell. LDOS calculations shows us that the AA-regions are indeed involved in the formation of flat bands. From the 2/3-metallic case [17] we learnt that, in particular, one AA-region per primitive cell induces the isolation of a group of eight central bands, with an inner subset of four remarkable flat bands. Our new findings confirm that this flattening happens irrespectively of the kind of tube, so that the number of isolated bands remains eight and four per AA-region in a primitive cell. Notice that there is no possibility of degeneration in the number of isolated bands, since we are considering primitive cells. Therefore, the AA-regions cannot be completely identical within a unit cell in spite of their striking similarity at first glance. Under this perspective, the increase of the dispersion in the location of narrow peaks in the DOS with increasing number of AA-regions, as shown in Fig. 8, seems fairly natural. Likewise, a bimodal structure of such distribution in the case of the Γ-metals matches comfortably with the zigzag structure of their moiré patterns. In fact, contrary to the 2/3-metals and semiconductor tubes, in the case of Γ-metals no band crosses the Fermi level even at the lowest moiré angle explored ($\theta_M = 0.95°$, (312,3) tube). These facts make the energy span criterion unreliable to find magic angles since now the flattest bands are not necessarily those closest to the Fermi level.

Notice also that there are pairs of semiconductors and Γ-metals sharing the same θ_M (see Fig. 7). In particular, that is the case for the (178,2) and (267,3) with $\theta_M = 1.11°$. Consistently the DOS criterium classifies both cases as “magic”, highlighting again the driving role of the moiré pattern in flat band engineering.

Multiplication of the DOS by the diameter of the corresponding nanotube does not change substantively the picture shown in Fig. 8: it enhances the 2/3-metallic CNT with respect the two other classes while balancing the performance between the semiconductor and the Γ-metallic CNTs. At any rate, there are no large differences; eventually, only experiments can tell whether some CNTs are better than others to explore one-dimensional strongly correlated behavior. Our work shows that moiré physics does not require chiral collapsed CNTs of an specific geometry other than being close to the universal magic angle ~1.1°.

Finally, for the reader’s convenience, we have collected in Table 1 the most relevant parameters characterizing all the nanotubes addressed in this work.

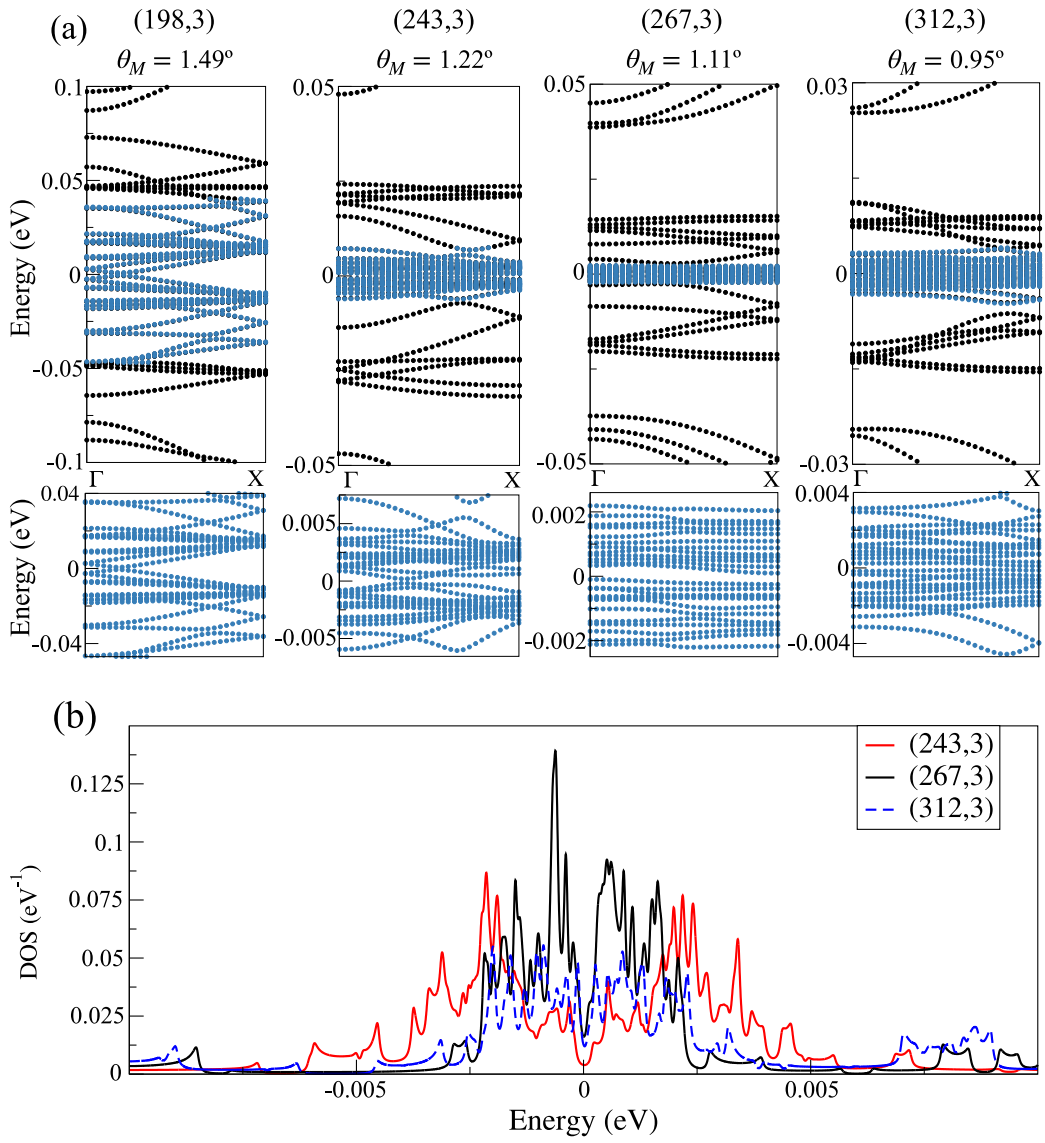

Fig. 5. (a) Band structures of four collapsed Γ-metal nanotubes. Mind the different energy scales. (b) DOS of the largest three nanotubes depicted in panel (a).

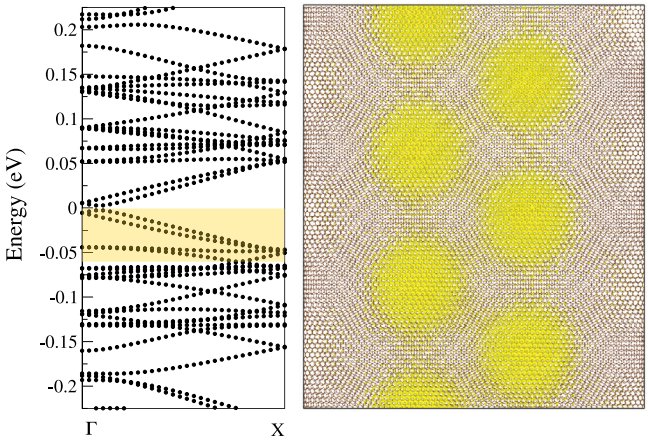

Fig. 6. Band structure and top view of the (132,3) Γ-metal nanotube. The LDOS of the marked bands is highlighted in yellow. (For interpretation of the references to color in this figure legend, the reader is referred to the web version of this article.)

5. Conclusions

We have analyzed the potential of all families of collapsed carbon nanotubes in flat-band engineering. The rotational symmetries of the uncollapsed tubes determine the structure of the moiré patterns. Thus, in their patterns, 2/3-metals show one AA-region per primitive cell, semiconductors have three in a linear arrangement, and Γ-metals present six in a zigzag disposition. Remarkably, the three families of collapsed CNTs display flat bands, high density of states and localization in the AA regions of the moiré when θ_M decreases. The number of highly flattened bands shows a perfect fourfold proportionality with the number of AA-regions per primitive cell, but otherwise, there are not significative differences. We have explored the criteria employed to find magic angles in moiré systems, namely, zero velocity, band span and high DOS, which were shown to yield the same result for 2/3 metals and TBG [17]. We have concluded that the DOS criterion is best suited to distinguish magic angle behavior in collapsed chiral CNTs of any type. In particular, the effects are maximized at the same magic moiré angle, namely ~1.1°.

Our results show that moiré physics is universal, i.e., it will appear in all kinds of chiral collapsed nanotubes, provided that their chiral angle is small enough to host AA-regions with localized states. This

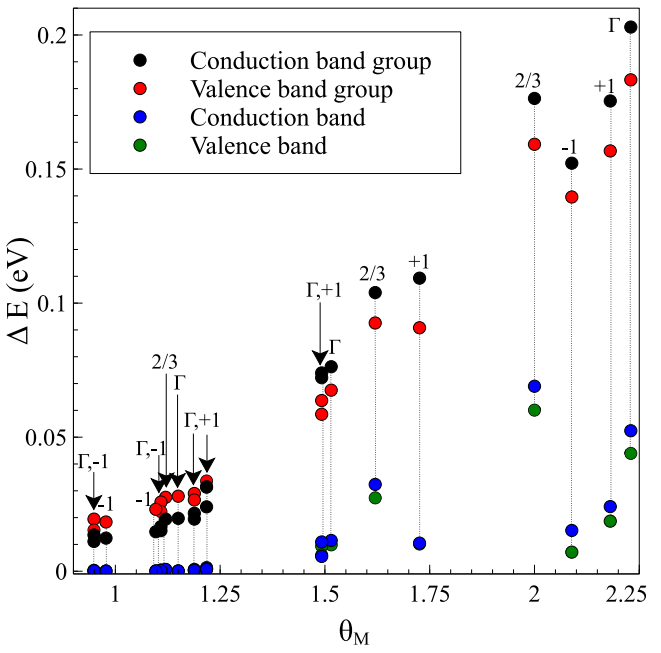

Fig. 7. Energy spans for the sets of flat bands in all kinds of CNTs. 2/3 and Γ-metals are labeled 2/3 and Γ, respectively, whereas the two subfamilies of semiconductors are labeled ±1. The energy widths of the pair of innermost bands, denoted by conduction and valence bands, is also shown.

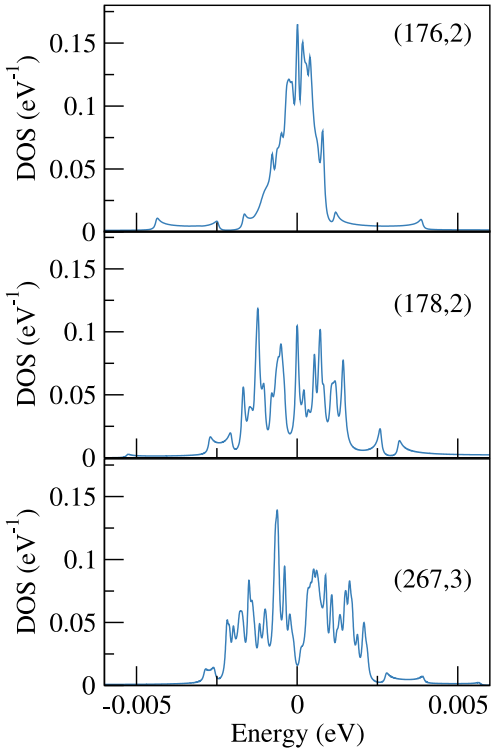

Fig. 8. From top to bottom: DOS around the Fermi energy of the 2/3-metal nanotube (176, 2) (θ_M = 1.12°), the semiconductor nanotube (178, 2) (θ_M = 1.11°) and the Γ-metal nanotube (267,3) (θ_M = 1.11°).

provides a new reliable perspective to approach other physical issues related to chiral collapsed CNTs, such as the twisting deformations of collapsed carbon nanotubes [52] and its potential relation with magic angles. We expect our conclusions to stir the experimental search for these one-dimensional, highly correlated systems.

Table 1
Data of the nanotubes that appear in all figures: family, moiré angle (θ_M), diameter of the cylindrical tube (d_{cyl}), length of the collapsed unit cell (T_{col}), number of moirés (N_M) and atoms (N_A) per unit cell.

(n,m)	Family	θ_M	d_{cyl} (Å)	T_{col} (Å)	N_M	N_A
(36,2)	SC	5.36	29.004	77.565	3	2 744
(132,3)	Γ	2.23	104.556	186.426	6	23 772
(90,2)	SC	2.18	71.270	190.603	3	16 568
(94,2)	SC	2.09	74.401	198.987	3	18 056
(98,2)	2/3	2.00	77.533	69.119	1	6 536
(114,2)	SC	1.73	90.060	240.864	3	26 456
(122,2)	2/3	1.62	96.324	85.872	1	10 088
(195,3)	Γ	1.52	153.881	274.378	6	51 492
(132,2)	SC	1.49	104.152	278.562	3	35 384
(198,3)	Γ	1.49	156.230	278.560	6	53 076
(162,2)	SC	1.22	127.642	341.390	3	53 144
(243,3)	Γ	1.22	191.464	341.414	6	79 716
(166,2)	SC	1.19	130.775	349.764	3	55 784
(249,3)	Γ	1.19	196.163	349.772	6	83 676
(258,3)	Γ	1.15	203.210	362.294	6	89 796
(176,2)	2/3	1.12	138.605	123.568	1	20 888
(178,2)	SC	1.11	140.170	374.898	3	64 088
(267,3)	Γ	1.11	210.256	374.870	6	96 132
(202,2)	SC	0.98	158.963	425.116	3	82 424
(208,2)	SC	0.95	163.661	437.724	3	87 368
(312,3)	Γ	0.95	245.492	437.748	6	131 052

CRediT authorship contribution statement

Olga Arroyo-Gascón: Conceptualization, Investigation, Writing. **Ricardo Fernández-Perea:** Software, Investigation. **Eric Suárez Morell:** Software, Investigation. **Carlos Cabrillo:** Conceptualization, Investigation, Writing. **Leonor Chico:** Conceptualization, Writing, Supervision.

Declaration of competing interest

The authors declare that they have no known competing financial interests or personal relationships that could have appeared to influence the work reported in this paper.

Acknowledgments

We thank Gloria Platero for generously sharing her computational resources and Sergio Bravo for helpful discussions. We also thank the Centro de Supercomputación de Galicia, CESGA, (www.cesga.es, Santiago de Compostela, Spain) for providing access to their supercomputing facilities. This work was supported by grant PID2019-106820RB-C21 funded by MCIN/AEI/ 10.13039/501100011033/ and by "ERDF A way of making Europe", by grant TED2021-129457B-I0 funded by MCIN/AEI/10.13039/501100011033/ and by the "European Union NextGenerationEU/PRTR" and by grant PRE2019-088874 funded by MCIN/AEI/10.13039/501100011033 and by "ESF Investing in your future". ESM acknowledges financial support from FONDECYT Regular, Chile 1221301, and LC gratefully acknowledges the support from Comunidad de Madrid (Spain) under the Multiannual Agreement with Universidad Complutense de Madrid, Program of Excellence of University Professors, in the context of the V Plan Regional de Investigación Científica e Innovación Tecnológica (PRICIT).

References

[1] E.Y. Andrei, D.K. Efetov, P. Jarillo-Herrero, A.H. MacDonald, K.F. Mak, T. Senthil, E. Tutuc, A. Yazdani, A.F. Young, The marvels of Moiré materials, Nat. Rev. Mater. 6 (2021) 201–206.

[2] T. Devakul, V. Crépel, Y. Zhang, L. Fu, Magic in twisted transition metal dichalcogenide bilayers, Nature Commun. 12 (2021) 6730.

[3] M.H. Naik, M. Jain, Ultraflatbands and shear solitons in Moiré patterns of twisted bilayer transition metal dichalcogenides, Phys. Rev. Lett. 121 (2018) 266401.

[4] Y. Cao, V. Fatemi, A. Demir, S. Fang, S.L. Tomarken, J.Y. Luo, J.D. Sanchez-Yamagishi, K. Watanabe, T. Taniguchi, E. Kaxiras, R.C. Ashoori, P. Jarillo-Herrero, Correlated insulator behaviour at half-filling in magic-angle graphene superlattices, Nature 556 (2018) 80–84.

[5] Y. Cao, V. Fatemi, S. Fang, K. Watanabe, T. Taniguchi, E. Kaxiras, P. Jarillo-Herrero, Unconventional superconductivity in magic-angle graphene superlattices, Nature 556 (2018) 43–50.

[6] P.K. Nayak, Y. Horbatenko, S. Ahn, G. Kim, J.-U. Lee, K.Y. Ma, A.-R. Jang, H. Lim, D. Kim, S. Ryu, H. Cheong, N. Park, H.S. Shin, Probing evolution of twist-angle-dependent interlayer excitons in $MoSe_2/WSe_2$ van der Waals Heterostructures, ACS Nano 11 (2017) 4041–4050.

[7] K. Tran, G. Moody, F. Wu, X. Lu, J. Choi, K. Kim, A. Rai, D.A. Sanchez, J. Quan, A. Singh, J. Embley, A. Zepeda, M. Campbell, T. Autry, T. Taniguchi, K. Watanabe, N. Lu, S.K. Banerjee, K.L. Silverman, S. Kim, E. Tutuc, L. Yang, A.H. MacDonald, X. Li, Evidence for Moiré excitons in van der Waals heterostructures, Nature 567 (2019) 71–75.

[8] F. Wu, T. Lovorn, E. Tutuc, A.H. MacDonald, Hubbard model physics in transition metal dichalcogenide Moiré bands, Phys. Rev. Lett. 121 (2018) 026402.

[9] A.M. León, É.A. Velásquez, F. Caro-Lopera, J. Mejía-López, Tuning magnetic order in CrI_3 bilayers via Moiré patterns, Adv. Theory Simul. 5 (2022) 2100307.

[10] E. Suárez Morell, J.D. Correa, P. Vargas, M. Pacheco, Z. Barticevic, Flat bands in slightly twisted bilayer graphene: Tight-binding calculations, Phys. Rev. B 82 (2010) 121407.

[11] Z. Song, Z. Wang, W. Shi, G. Li, C. Fang, B.A. Bernevig, All magic angles in twisted bilayer graphene are topological, Phys. Rev. Lett. 123 (2019) 036401.

[12] M. Serlin, C.L. Tschirhart, H. Polshyn, Y. Zhang, J. Zhu, K. Watanabe, T. Taniguchi, L. Balents, A.F. Young, Intrinsic quantized anomalous Hall effect in a Moiré heterostructure, Science 367 (2020) 900–903.

[13] G. Tarnopolsky, A.J. Kruchkov, A. Vishwanath, Origin of magic angles in twisted bilayer graphene, Phys. Rev. Lett. 122 (2019) 106405.

[14] S. Lisi, X. Lu, T. Benschop, T.A. de Jong, P. Stepanov, J.R. Duran, F. Margot, I. Cucchi, E. Cappelli, A. Hunter, A. Tamai, V. Kandyba, A. Giampietri, A. Barinov, J. Jobst, V. Stalman, M. Leeuwenhoek, K. Watanabe, T. Taniguchi, L. Rademaker, S.J. van der Molen, M.P. Allan, D.K. Efetov, F. Baumberger, Observation of flat bands in twisted bilayer graphene, Nat. Phys. 17 (2021) 189–193.

[15] M.N. Huda, S. Kezilebieke, P. Liljeroth, Designer flat bands in quasi-one-dimensional atomic lattices, Phys. Rev. Res. 2 (2020) 043426.

[16] D.M. Kennes, L. Xian, M. Claassen, A. Rubio, One-dimensional flat bands in twisted bilayer germanium selenide, Nature Commun. 11 (2020) 1124.

[17] O. Arroyo-Gascón, R. Fernández-Perea, E. Suárez Morell, C. Cabrillo, L. Chico, One-dimensional Moiré superlattices and flat bands in collapsed chiral carbon nanotubes, Nano Lett. 20 (2020) 7588–7593.

[18] S. Zhao, R. Kitaura, P. Moon, M. Koshino, F. Wang, Interlayer interactions in 1D Van der Waals Moiré superlattices, Adv. Sci. 9 (2022) 2103460.

[19] R. Bonnet, A. Lherbier, C. Barraud, M.L.D. Rocca, P. Lafarge, J.-C. Charlier, Charge transport through one-dimensional Moiré crystals, Sci. Rep. 6 (2016) 19701.

[20] S. Zhao, P. Moon, Y. Miyauchi, T. Nishihara, K. Matsuda, M. Koshino, R. Kitaura, Observation of drastic electronic-structure change in a one-dimensional Moiré superlattice, Phys. Rev. Lett. 124 (2020) 106101.

[21] M. Koshino, P. Moon, Y.-W. Son, Incommensurate double-walled carbon nanotubes as one-dimensional Moiré crystals, Phys. Rev. B 91 (2015) 035405.

[22] M.S. Dresselhaus, G. Dresselhaus, A. Jorio, Group Theory: Application to the Physics of Condensed Matter, Springer-Verlag, Berlin, 2008.

[23] N.G. Chopra, L.X. Benedict, V.H. Crespi, M.L. Cohen, S.G. Louie, A. Zettl, Fully collapsed carbon nanotubes, Nature 377 (1995) 135–138.

[24] L.X. Benedict, N.G. Chopra, M.L. Cohen, A. Zettl, S.G. Louie, V.H. Crespi, Microscopic determination of the interlayer binding energy in graphite, Chem. Phys. Lett. 286 (1998) 490–496.

[25] T. Tang, A. Jagota, C.-Y. Hui, N.J. Glassmaker, Collapse of single-walled carbon nanotubes, J. Appl. Phys. 97 (2005) 074310.

[26] G. Gao, T. Çagin, W.A. Goddard, Energetics, structure, mechanical and vibrational properties of single-walled carbon nanotubes, Nanotechnology 9 (1998) 184–191.

[27] H.J. Liu, K. Cho, A molecular dynamics study of round and flattened carbon nanotube structures, Appl. Phys. Lett. 85 (2004) 807–809.

[28] J.A. Elliott, J.K.W. Sandler, A.H. Windle, R.J. Young, M.S.P. Shaffer, Collapse of single-wall carbon nanotubes is diameter dependent, Phys. Rev. Lett. 92 (2004) 095501.

[29] C. Zhang, K. Bets, S.S. Lee, Z. Sun, F. Mirri, V.L. Colvin, B.I. Yakobson, J.M. Tour, R.H. Hauge, Closed-edged graphene nanoribbons from large-diameter collapsed nanotubes, ACS Nano 6 (2012) 6023–6032.

[30] M. He, J. Dong, K. Zhang, F. Ding, H. Jiang, A. Loiseau, J. Lehtonen, E.I. Kauppinen, Precise determination of the threshold diameter for a single-walled carbon nanotube to collapse, ACS Nano 8 (2014) 9657–9663.

[31] A. Impellizzeri, P. Briddon, C.P. Ewels, Stacking- and chirality-dependent collapse of single-walled carbon nanotubes: A large-scale density-functional study, Phys. Rev. B 100 (2019) 115410.

[32] M. He, J. Dong, H. Wang, H. Xue, Q. Wu, B. Xin, W. Gao, X. He, J. Yu, H. Sun, F. Ding, J. Zhang, Advance in close-edged graphene nanoribbon: Property investigation and structure fabrication, Small 15 (2019) 1804473.

[33] G. Trambly de Laissardière, D. Mayou, L. Magaud, Localization of Dirac electrons in rotated graphene bilayers, Nano Lett. 10 (2010) 804–808.

[34] R. Saito, M. Fujita, G. Dresselhaus, M.S. Dresselhaus, Electronic structure of chiral graphene tubules, Appl. Phys. Lett. 60 (1992) 2204–2206.

[35] N. Hamada, S.-i. Sawada, A. Oshiyama, New one-dimensional conductors: Graphitic microtubules, Phys. Rev. Lett. 68 (1992) 1579–1581.

[36] R. Saito, M. Fujita, G. Dresselhaus, M.S. Dresselhaus, Electronic structure of graphene tubules based on C 60, Phys. Rev. B 46 (1992) 1804–1811.

[37] M. Damnjanović, I. Milošsević, Line Groups in Physics, in: Lecture Notes in Physics, vol. 801, Springer Berlin Heidelberg, Berlin, Heidelberg, 2010, http://dx.doi.org/10.1007/978-3-642-11172-3.

[38] A. Skurativska, S.S. Tsirkin, F.D. Natterer, T. Neupert, M.H. Fischer, Flat bands with fragile topology through superlattice engineering on single-layer graphene, Phys. Rev. Res. 3 (2021) 032003.

[39] R. Okuyama, W. Izumida, M. Eto, Topological classification of the single-wall carbon nanotube, Phys. Rev. B 99 (2019) 115409.

[40] B. Bradlyn, L. Elcoro, J. Cano, M.G. Vergniory, Z. Wang, C. Felser, M.I. Aroyo, B.A. Bernevig, Topological quantum chemistry, Nature 547 (2017) 298–305.

[41] I. Milošević, S. Dmitrović, T. Vuković, A. Dimić, M. Damnjanović, Elementary band representations for (double)-line groups, J. Phys. A 53 (2020) 455204.

[42] A.P. Thompson, H.M. Aktulga, R. Berger, D.S. Bolintineanu, W.M. Brown, P.S. Crozier, P.J. in't Veld, A. Kohlmeyer, S.G. Moore, T.D. Nguyen, R. Shan, M.J. Stevens, J. Tranchida, C. Trott, S.J. Plimpton, LAMMPS - a flexible simulation tool for particle-based materials modeling at the atomic, meso, and continuum scales, Comput. Phys. Comm. 271 (2022) 108171.

[43] M.M. van Wijk, A. Schuring, M.I. Katsnelson, A. Fasolino, Relaxation of Moiré patterns for slightly misaligned identical lattices: Graphene on graphite, 2D Mater. 2 (2015) 034010.

[44] S.J. Stuart, A.B. Tutein, J.A. Harrison, A reactive potential for hydrocarbons with intermolecular interactions, J. Chem. Phys. 112 (2000) 6472–6486.

[45] N.N.T. Nam, M. Koshino, Lattice relaxation and energy band modulation in twisted bilayer graphene, Phys. Rev. B 96 (2017) 075311.

[46] J.M. Soler, E. Artacho, J.D. Gale, A. García, J. Junquera, P. Ordejón, D. Sánchez-Portal, The SIESTA method for ab initio order- N materials simulation, J. Phys.: Condens. Matter 14 (2002) 2745–2779.

[47] N. Troullier, J.L. Martins, Efficient pseudopotentials for plane-wave calculations, Phys. Rev. B 43 (1991) 1993–2006.

[48] J.P. Perdew, K. Burke, M. Ernzerhof, Generalized gradient approximation made simple, Phys. Rev. Lett. 77 (1996) 3865–3868.

[49] H. Kataura, Y. Kumazawa, Y. Maniwa, I. Umezu, S. Suzuki, Y. Ohtsuka, Y. Achiba, Optical properties of single-wall carbon nanotubes, Synth. Met. 103 (1999) 2555–2558.

[50] L. Chico, M.P. López-Sancho, M.C. Muñoz, Curvature-induced anisotropic spin–orbit splitting in carbon nanotubes, Phys. Rev. B 79 (2009) 235423.

[51] J.-C. Charlier, X. Blase, S. Roche, Electronic and transport properties of nanotubes, Rev. Modern Phys. 79 (2007) 677–732.

[52] H.R. Barzegar, A. Yan, S. Coh, E. Gracia-Espino, C. Ojeda-Aristizabal, G. Dunn, M.L. Cohen, S.G. Louie, T. Wågberg, A. Zettl, Spontaneous twisting of a collapsed carbon nanotube, Nano Res. 10 (2017) 1942–1949.